

Tip-Enhanced Raman Spectroscopic Imaging of Individual Carbon Nanotubes with Subnanometer Resolution

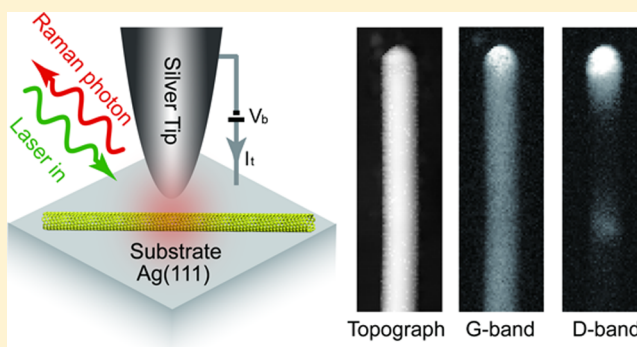
Menghan Liao, Song Jiang, Chunrui Hu, Rui Zhang, Yanmin Kuang, Jiazhe Zhu, Yang Zhang, and Zhenchao Dong*

Hefei National Laboratory for Physical Sciences at the Microscale and Synergetic Innovation Center of Quantum Information & Quantum Physics, University of Science and Technology of China, Hefei, Anhui 230026, China

S Supporting Information

ABSTRACT: Individual carbon nanotubes (CNTs) have been investigated by tip-enhanced Raman spectroscopy (TERS) using silver tips on the Ag(111) substrate with a low-temperature ultrahigh-vacuum scanning tunneling microscope. Thanks to the strong and highly localized plasmonic field offered by the silver nanogap, the spatial resolution of TERS on CNTs is driven down to about 0.7 nm. Such a high spatial resolution allows to visualize in real space the spatial extent of the defect-induced D-band scattering, to track the strain-induced spectral evolution, and to resolve the spectral differences between the inner and the outer sides of a bent CNT, all at the nanometer scale.

KEYWORDS: Tip-enhanced Raman spectroscopy (TERS), carbon nanotubes (CNTs), nanoimaging, defects, strain



Accessing chemical information on individual nanostructures such as carbon nanotubes (CNTs) with high spatial resolution is important for understanding their structure and property as well as for their applications in nanodevices.^{1–3} Tip-enhanced Raman spectroscopy (TERS) offers an attractive approach to this end due to its combined advantage of ultrahigh spatial resolution in scanning probe microscopy and sensitive chemical specificity of vibrational fingerprints in Raman scattering.^{4–11} CNTs have been used as a classical material to demonstrate the power and development of TERS^{12–21} thanks to their large Raman scattering cross section and structural stability on surfaces under laser illumination. Earlier TERS experiments of CNTs were conducted under an atomic force microscope (AFM) in ambient with a typical spatial resolution of 10–20 nm.^{12–16} Higher spatial resolutions of about 3–4 nm were obtained with AFM-TERS by applying force¹⁷ or time-gated illumination.¹⁸ Recently, the spatial resolution of TERS on CNTs has been driven down to ~1.7 nm by using a scanning tunneling microscope (STM) in ambient with gold tip and substrate.¹⁹ However, despite these progresses, there are still important issues to be clarified. For example, can the spatial resolution of TERS on the CNT nanostructure be further improved to the subnanometer level as recently demonstrated for porphyrin molecules?^{10,11} Can the higher resolution provide more insights into the behavior of defects and strain in a CNT?^{15,16}

In this paper, we shall address these issues by performing STM-controlled TERS experiments on CNTs with silver (Ag) tip and Ag(111) substrate (Figure 1a). The selection of silver as both tip and substrate materials in this work is to explore the

limit of plasmonic confinement and enhancement effect for this system since silver is known as the best plasmonic material owing to its lowest optical losses at visible and near-infrared frequencies compared with other metals.^{22,23}

Our TERS experiments were performed with a custom low-temperature ultrahigh-vacuum (UHV) STM under a base pressure of $\sim 1 \times 10^{-10}$ Torr at ~ 79 K, equipped with a side-illumination confocal optical system, as shown in Figure S1 in Supporting Information (SI). CVD grown single wall carbon nanotubes (CNTs) (Nanjing XFNANO Materials Tech Co., Ltd.) were used as received without further purification. The sample for TERS experiments was prepared by the dry contact transfer (DCT) method in UHV,²⁴ which could prevent the sample from contamination and oxidation, and thus ensure the deposition of well-defined CNT structures on a clean Ag(111) surface. The CNT powder was first dispersed in 1,2 dichloroethane solution (0.5 mg/mL). Upon supersonic bathing for 30 min, a small amount of the liquid solution was dropped onto clean glass fiber braids that were mounted on a sample holder and previously degassed in UHV. Then the braids were carefully manipulated to contact gently with the Ag(111) surface of a silver single crystal. In this way, some CNTs were transferred from the glass fibers to the Ag(111) surface, yielding a sample with both isolated single CNTs and aggregated CNT bundle clusters. The CNT sample was further

Received: February 5, 2016

Revised: May 31, 2016

Published: June 27, 2016

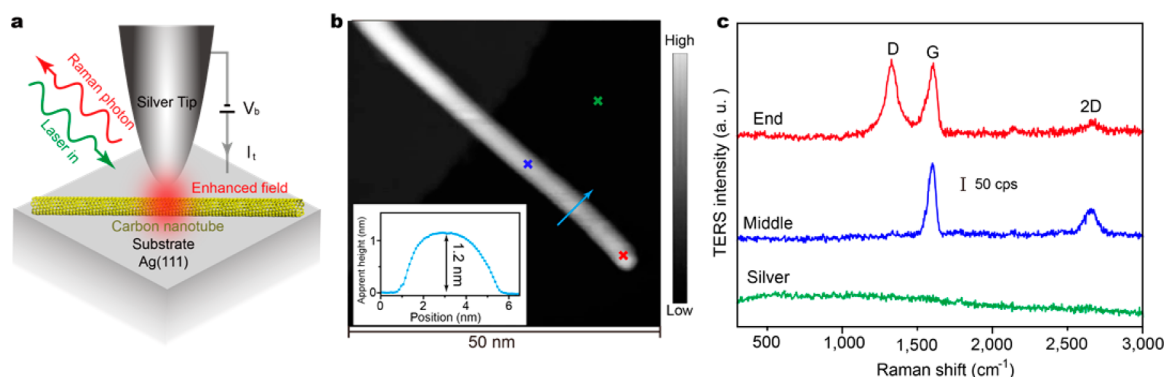


Figure 1. (a) Schematic illustration of the STM-TERS experiments. (b) STM topograph of an isolated CNT on Ag(111) (1 V, 10 pA). Inset: Line profile of the CNT along the blue arrow line. Due to the tip convolution related to the tip shape and size, the CNTs are broadened to about 4.5 nm.²⁵ (c) TERS spectra (0.1 V, 500 pA, 20 s) acquired at the corresponding positions marked in part b. All of the TERS spectra in this work were corrected by subtracting the constant far-field signals when the tip was retracted by ~ 400 nm.

annealed around 350 °C for 5 min and then transferred to the observation chamber for STM and TERS experiments.

Figure 1b shows a STM topograph of a sample thus prepared, featuring an isolated single CNT lying straight on the Ag(111) surface. The diameter of the CNT can be estimated to be ~ 1.2 nm from the apparent height in the STM topograph (the inset of Figure 1b).^{19,25} As shown in Figure 1c, when a silver tip is positioned above a CNT, the TERS signals are not only strongly enhanced in comparison with the far-field signals when the tip is retracted, but also site-dependent with significant spectral changes from the tube end to the middle. At the end of the CNT, we can observe the tangential G-band (~ 1600 cm^{-1}) associated with C=C stretching vibrations, the defect-induced D-band (~ 1350 cm^{-1}) associated with a dispersive phonon mode, and the second-order 2D-band (~ 2700 cm^{-1}) that involves a two-phonon process, in agreement with the literature.^{26,27} Whereas at the middle of the CNT, only the G-band and 2D-band are observed by TERS. It should be pointed out that all TERS spectra given here have been subtracted by the far-field Raman signals, as detailed in Figure S2 in SI. Unexpectedly, the signal from the radial breath mode (RBM) is very weak in our TERS experiments of CNTs on Ag(111) (see Figures S2 and S3 in SI), which is different from previous TERS reports of CNTs on glass substrates,^{13,14,20} probably due to the stronger interaction between CNTs and metal substrates. Note that when the tip is placed on the bare Ag surface near a CNT, no Raman signals can be observed except for a broad featureless continuum associated with the inelastic scattering of the plasmonic nanocavity. These observations have several implications: (1) the tip is not contaminated, (2) the plasmonic confinement underneath the tip is down to a very local scale, and (3) the “far-field” signals from CNTs when the tip is positioned on the bare Ag are essentially the same as the far-field signals when the tip is retracted by about 400 nm. All of these implications give further justification that the Raman signals observed in the top two spectra of Figure 1c are truly the near-field enhanced signals from the very local portion of the CNT underneath the tip. The TERS enhancement factor for the G-band of a CNT on Ag(111) with Ag tips, a nontrivial issue in TERS studies, is estimated to be as large as $\sim 10^8$, as detailed in Figure S4 in SI.

In order to get a panoramic view of the spatial distribution of different Raman bands, spatially resolved TERS imaging over an isolated CNT with high pixel resolution (with each pixel recording a TERS spectrum during raster scanning) was carried

out. Figure 2a shows the STM topograph (left panel) of a selected CNT and simultaneously acquired TERS images for the G-band (middle panel) and the D-band (right panel), respectively, with hitherto highest pixel resolution over a single CNT (0.25 nm/pixel). The latter two images are spectrally

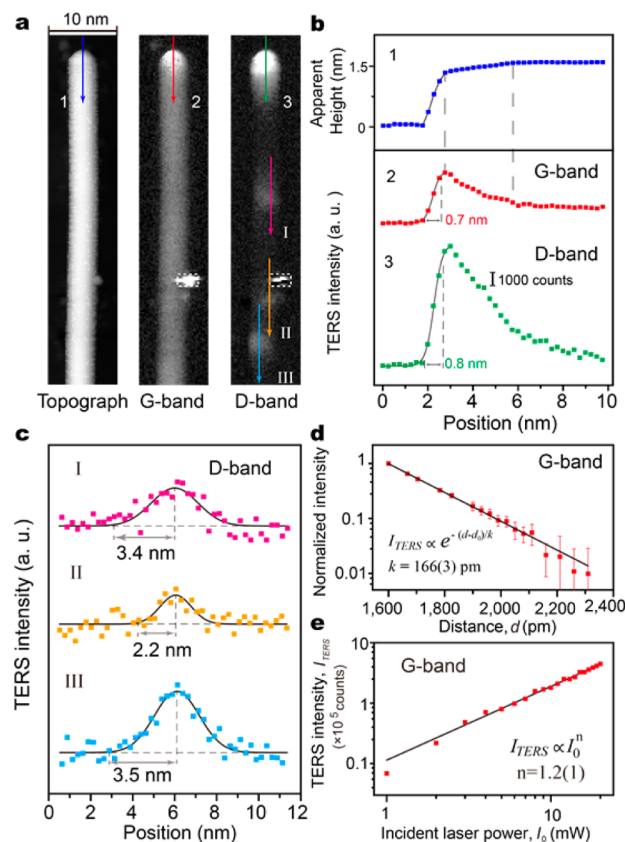


Figure 2. (a) Simultaneously acquired STM topograph and TERS mappings for the G-band (1450–1650 cm^{-1}) and D-band (1200–1450 cm^{-1}) of a CNT, respectively (0.1 V, 500 pA, 10×50 nm², 40×200 pixels, 0.3 s/pixel). The bright feature inside the rectangle marked in panel a is identified as amorphous carbon cluster impurity. (b, c) Apparent height profile and TERS intensity profiles along the arrow lines marked in panel a, respectively. (d) Dependence of the normalized net G-band intensity (I_{TERS}) on the gap distance (d). (e) Dependence of the net G-band intensity (I_{TERS}) on the incident laser power (I_0) (0.1 V, 500 pA, 20 s).

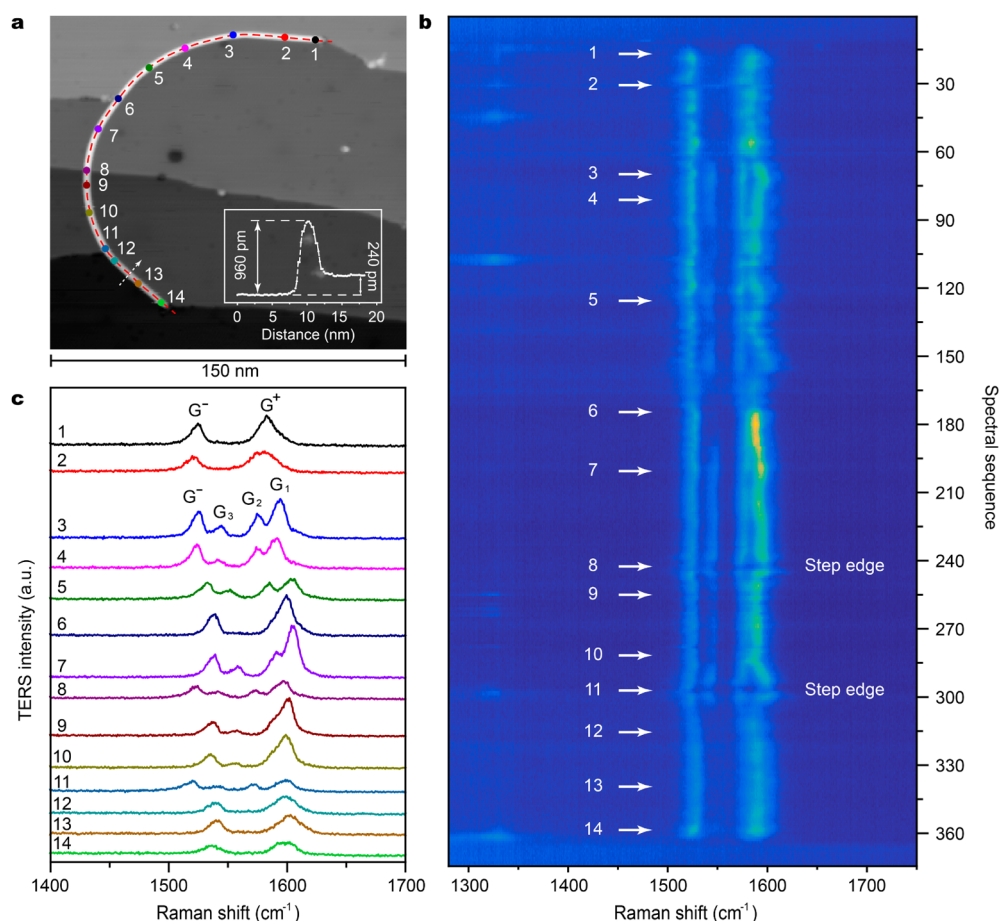


Figure 3. (a) STM topograph of an as-found bent CNT on Ag(111) with a length of about 210 nm (1.8 V, 5 pA). Inset: line profile at the white arrowed line. (b) A series of TERS spectra acquired along the red dashed line in (a) (1.0 V, 100 pA, 10 s). (c) Representative TERS spectra at the corresponding positions marked in a and extracted from b.

reconstructed by integrating the Raman signals over the corresponding peaks from the spectrum measured at each pixel.

Unlike the nearly uniform brightness feature of the CNT in the STM topograph, the TERS images provide more structural information about the CNT in terms of contrast variations, particularly for the defect-induced D-band. Before we discuss in detail, let us see what kind of spatial resolution has been achieved in the current system. According to the estimation based on the 10–90% optical contrast, the TERS intensity profiles along the marked arrow lines near the tube end exhibit a spatial resolution down to the subnanometer regime, about 0.7 nm for the G-band (line 2) and 0.8 nm for the D-band (line 3), respectively (Figure 2b). Such an ultrahigh resolution allows us not only to view better the spatial distributions of the G-band and D-band, but also to chemically identify the tiny impurity attached to the CNT (marked inside the rectangle in Figure 2a) as amorphous carbon clusters (see Figure S5 in SI for more details).

There are two evident features in the TERS images of Figure 2a: (1) the very strong Raman signals at the tube end for the defect-induced D-band and (2) the overall uniform distribution of significant Raman signals throughout the tube for the tangential G-band. The former indicates a very high density of defects at the tube end, while the latter justifies that the G-band signals are not originated from defects. Nevertheless, the G-band signals also become stronger close to the tube end, though the contrast is not as sharp as that for the D-band there

(lines 2 and 3 in Figure 2b). According to the apparent heights shown in line 1 of Figure 2b, the diameter of the CNT becomes smaller toward the tube end. Therefore, the increase in the G-band intensity toward the CNT end appears related to either the stronger nanocavity–plasmon strength due to the decreased tip–substrate distances¹⁸ or different resonance conditions with the 532 nm laser owing to the change of local density of states of the CNT,²⁸ or both.

Of particular interest is the observation of certain scattered D-band signals far away from the tube end (marked by arrow lines I–III in Figure 2a), which suggests the presence of defects in the corresponding areas. In spite of relatively localized nature of point-like defects in a CNT such as pentagons, heptagons, vacancies, or dopant,² the D-band signals are found spatially extended into a small area with certain sizes (Figure 2a, c). In other words, even when the silver tip is not placed right above the point-like defects, the D-band signals can still be activated around the defects within a certain length scale. Such a length scale can be called the relaxation length of the D-band scattering near a defect, which is closely related to the distance over which the photoexcited electron–hole pair can travel to a nearby defect during its lifetime and also be scattered.^{15,29–35} If we use a Gaussian function to fit the three TERS intensity profiles for the D-band along the arrow lines I–III in Figure 2a, the half of the full width can be approximately viewed as the radius of the D-band activation zone, which ranges from 2.2 to 3.5 nm (Figure 2c). Different activation radii may be associated

with different numbers of defects contained or different types of defects involved or both. Since even the smallest D-band extent contains at least one defect, the observed 2.2 nm can be considered as the upper limit of the relaxation length of the D-band scattering near such a defect, which is similar to those reported previously for CNTs and graphene (but estimated based on indirect and complex analyses).^{15,31–35} Thanks to the subnanometer resolution of our TERS technique, we are able to view the D-band extent and measure its relaxation length directly in real space.

The origin of the subnanometer resolution is believed to correlate with the highly confined plasmonic field inside the STM junction,^{10,11,36–39} although the exact mechanism is still not completely clear. From the phenomenological point of view, the ultrahigh spatial resolution is related to the rapid exponential decay of the TERS signals with the increased gap-distance between the tip and the substrate, as shown in Figure 2d (see Figure S6 in SI for more details). The exponential decay factor of 166(3) pm here is about 7 times smaller than that of CNTs on Au(111) using gold tips,¹⁹ which may imply a more localized plasmonic field and thus a higher spatial resolution in the case of using the silver material. The physical mechanism behind the subnanometer spatial resolution may also pertain to the nonlinear behavior of plasmon-enhanced Raman signals in the STM nanocavity.^{10,11} A power-law fitting for the dependence of the net G-band signals on the incident laser power gives rise to an exponent of 1.2(1) (Figure 2e), which indicates the involvement of high-order Raman processes other than the spontaneous linear Raman scattering, as discussed previously in refs 10 and 11. However, in the case of CNTs, such a power-law exponent is smaller than that reported for H₂TBPP and ZnTPP molecules,^{10,11} which is consistent with the slightly larger exponential decay factor and slightly lower spatial resolution here. It should be noted that the slightly poorer specifications for the CNTs with respect to the porphyrin molecules may arise from the slightly larger gap-distance between the tip and substrate and resultant less confined and less intense plasmonic fields in the case of CNTs.

The improved subnanometer resolution on CNTs not only enables a clearer view of how defects affect the D-band scattering and their spatial distribution, as demonstrated above but also allows us to fine track the spectral evolution induced by strain in a CNT with better resolution. Since the nondispersive G-band structure is known sensitive to the strain variations,^{16,40–45} we will focus on the spectral variations of the G-band in the following.

Figure 3a shows a bent CNT as-found on Ag(111) after annealing but without artificial manipulation. A series of TERS spectra were acquired sequentially along the bent CNT with a small step size of 0.4–0.8 nm to fine track the influence of strain on the spectral profile of the G-band, as shown in Figure 3b. The most dominant feature is the coexistence of both two-peak and four-peak G-band structures within the same CNT, as highlighted in the representative spectra in Figure 3c. For the TERS spectra over the straight portions (e.g., from position 1 to 2 and from position 12 to 14), the G-band of the CNT shows a two-peak structure, with the axial G⁺ mode at ~1585 cm⁻¹ and the circumferential G⁻ mode at ~1524 cm⁻¹.^{16–20} For the bent portions (e.g., from position 3 to 5 and from position 7 to 11), the G⁺ band is found to split into two peaks with blue-shifted G₁ and red-shifted G₂, thus reflecting its sensitivity to the strain caused by bending. On the other hand, no evident splitting was observed for the G⁻ mode along the

CNT, though the peak positions were found to swing around (1519–1530 cm⁻¹) together with the G⁺ or G₂ mode. In addition, a new peak labeled as G₃ emerges, presumably originated from the strain caused by bending, as theoretically predicted in ref 44.

The G-band spectral feature could also be affected by the local environment. The TERS intensities for the CNT portions attached to and across the step edges (e.g., from position 1 to 6, position 8, position 11, and position 11 to 14) are generally weaker than those portions lying on the flat terraces, which is probably due to weaker plasmonic field strength at the step edges.⁴⁶ In addition, the G⁺ band across the step edges (position 8 and 11) is found to be further split presumably owing to the additional bending caused by the step edges (Figure 3b). It is worth noting that the subnanometer TERS resolution enables us to fine track the complex spectral variations along the CNT, including the transitions from the two-peak to four-peak feature, the peak position swinging, and the sharp intensity changes across the step edges within ~2 nm (Figure 3b), thus demonstrating the power of ultrahigh spatial resolution in revealing the sensitive dependence of TERS on the local nanostructure and environment.

We would like to note that the CNT shown in Figure 3 is not in resonance with the excitation laser at 532 nm, according to the gaps of van Hove singularities observed in the scanning tunneling spectroscopy measurements (see Figure S7 in SI for more information). Nevertheless, we still observed TERS signals with good signal-to-noise ratios (Figure 3b and c).

As shown above, the spectral variations observed along the as-found bent CNT is very complex due to different strains caused by the bending and the interactions with the substrate. In order to specifically examine the effect of the bending induced strain on TERS spectra, we artificially create a bent CNT by cutting and manipulating a straight CNT with a Ag tip (Figure 4a and b), using technical approaches reported previously.^{16,41,47} We would like to note that an elegant study on the global behavior of strain in CNTs was reported in ref 16, though with a relatively low spatial resolution of about 20 nm. For cutting, we positioned the tip above a selected site on a CNT and applied a voltage pulse (30 ms, 7 V) at a tunneling current of 100 pA. For pushing, we first positioned the tip on the bare silver surface next to a CNT, then lowered the tip down by about 0.8 nm (with the feedback loop switched off), and finally moved the tip to push the CNT to the desired location nearby. (After manipulation, the tip was seriously damaged and no longer TERS active. But thanks to the clean and stable conditions offered by the low-temperature UHV environment, we can modify the tip status in situ on the bare silver surface by applying voltage pulses to regain TERS activity.)

Figure 4b shows one example created by such manipulation procedure with one portion of an excised CNT pushed into a curly S-shape. For the representative TERS spectra acquired from the straight CNT before manipulation (Figure 4c), the spectral features are essentially the same in terms of peak numbers and positions. However, the four-peak feature observed here is different from the two-peak feature observed in the straight portion of the as-found CNT in Figure 3. The reason behind the spectral difference is still unknown but might be related to the different chiral structures of the CNTs.^{48,49} By contrast, the TERS spectrum from the bent portion of the CNT after manipulation (as exemplified in the red curve in Figure 4d) presents an evidently different spectral profile

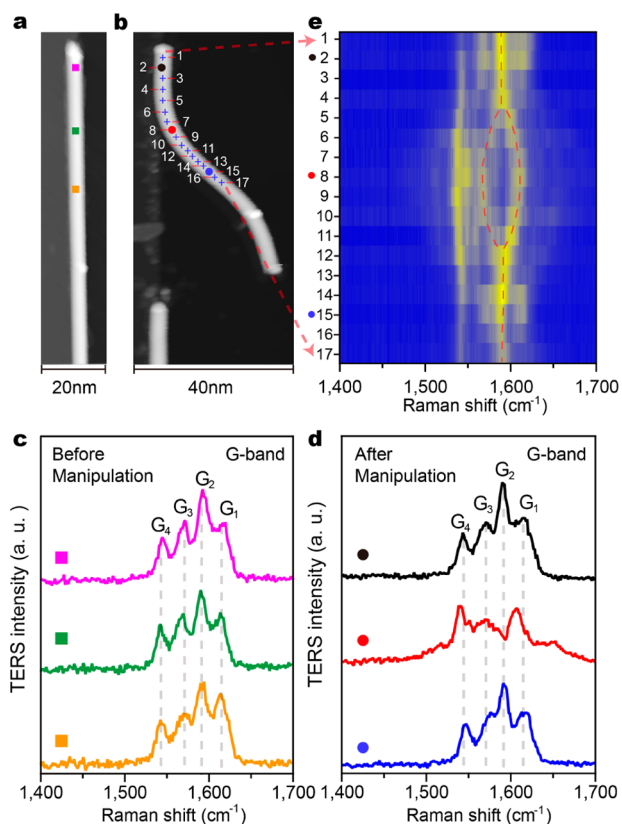


Figure 4. STM topograph of an isolated CNT before (a) and after (b) manipulation (1 V, 10 pA), respectively, with an image size of $20 \times 100 \text{ nm}^2$ for panel a and $40 \times 80 \text{ nm}^2$ for panel b. (c–e) TERS spectra (0.1 V, 500 pA, 360 s) acquired at the positions marked in panels a and b.

compared with that acquired from the corresponding position before manipulation (the green curve in Figure 4c).

In order to track the TERS spectral evolution due to the artificial bending, a series of TERS spectra were then acquired sequentially along the bent CNT with a step size of 1.8–3.0 nm. These spectra are plotted in Figure 4e and exhibit clearly the spectral shift and splitting of the G-band signals of a CNT upon bending. The first four spectra acquired from the straight portion of the excised CNT show similar four-peak structures to those spectra in Figure 4c measured before manipulation, which reflects a nearly bending-free nature for this portion of

the CNT. However, starting from the fifth spectrum (position 5), pronounced changes start to emerge. The G_2 peak at $\sim 1590 \text{ cm}^{-1}$ starts to split into two branches, as marked with dashed lines in Figure 4e. Along with the decrease of the curvature radius and the resultant increase of the strain, the G_2 peak is further split, reaching a maximum at position 8 where the strain is highest due to the smallest curvature radius there. Then, from position 9 to 13, the splitting becomes smaller and smaller and finally merges together. The last four positions (14 to 17) show again essentially the same spectra as those for the straight CNT before manipulation. Overall speaking, the bending induced strain can result in the splitting of the G-band: the smaller the curvature radius is, the larger the splitting. Notably, the G-band splitting here is probably not caused by the pressure from the STM tip under current experimental conditions, since the normalized TERS spectra are practically the same for different tip–substrate distances (see Figure S8 in SI for more details). We would like to note that sophisticated theoretical studies are desirable for a better understanding on the diversity and complexity of spectral features observed experimentally in individual CNTs, as exemplified in Figures 3 and 4.

Since the bending of a CNT will result in both the stretching of the axial C=C bond on the outer side and the bond compression on the inner side, the vibrational signals detected from different sides are expected to be different. Indeed, the subnanometer resolution in our STM-controlled TERS enables us to resolve such differences in a bent CNT. Figure 5a shows another artificially bent CNT with a diameter of $\sim 1.5 \text{ nm}$ on Ag(111) estimated from the apparent height. The normalized TERS spectra measured from the inner (P1) or outer (P2) sides of the straight portion show essentially the same spectral profile, as illustrated in Figure 5b. However, for the bent portion, the normalized TERS spectrum for the inner side (P3), compared with that for the outer side (P4), exhibits a pronounced increase in the relative intensity of G_1 with respect to G_2 , apart from the evident blue-shift of G_1 and red-shift of G_2 due to bending. Although both G_1 and G_2 modes are observed from inner and outer sides, the difference in the relative intensity (namely, the G_1/G_2 ratio) suggests different amounts of contributions from the inner and outer vibrations for a bent CNT. Specifically, for the blueshifted G_1 mode, the observed increased G_1/G_2 ratio acquired at the inner side suggests that the G_1 mode is more related to the inner compressed vibrations; whereas for the red-shifted G_2 mode, the observed decreased G_1/G_2 ratio acquired at the outer side

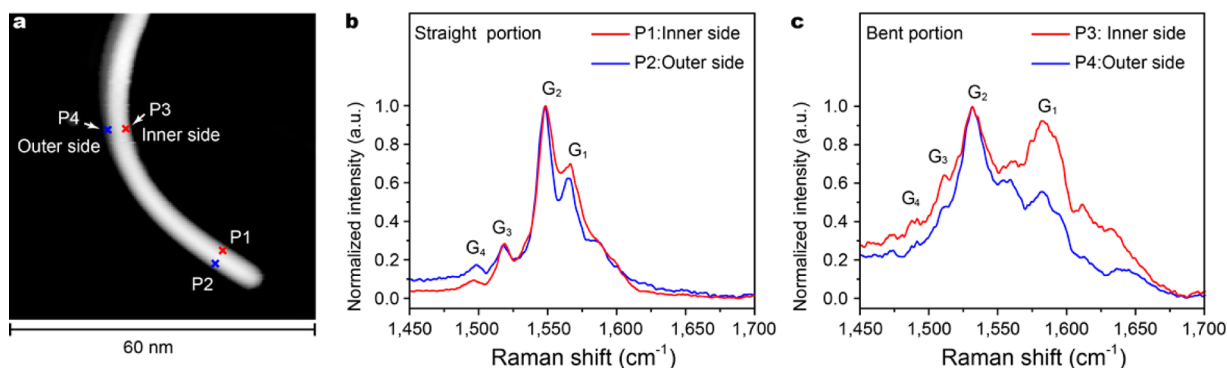


Figure 5. (a) STM topograph of an isolated CNT after manipulation (2 V, 5 pA). (b and c) TERS spectra (0.5 V, 100 pA, 60 s) acquired at the corresponding positions marked in panel a. In order to show the spectral differences, the TERS spectra here were normalized by the intensities of the strongest emission peaks.

suggests that the G_2 mode is more related to the outer stretched vibrations.

In summary, we have investigated the STM-controlled TERS spectra of isolated single CNTs on Ag(111) using Ag tips. The selection of Ag as both tip and substrate materials is found to produce a large TERS enhancement factor up to about 10^8 , originating from the strong enhancement of gap-mode plasmons. The highly confined plasmonic field in the nanogap also drives the spatial resolution of TERS imaging on a CNT down to about 0.7 nm. Such subnanometer resolution allows us not only to visualize directly the spatial extent of defect-induced D-band scattering in real space, but also to fine track the spectral evolution of the G-band with the strain variations due to the bending and the local environment. Furthermore, the ability to resolve the TERS spectral difference between the inner and the outer sides of a bent CNT helps to provide insights into the origin of G-band. To put it in perspective, our results demonstrate that TERS can go beyond chemical identification and serve as a powerful tool to investigate the defect and strain in low dimensional nanostructures and materials at the subnanometer scale. Such ability can help to understand, design, and control the performance of nanoscale materials and devices.

■ ASSOCIATED CONTENT

Supporting Information

The Supporting Information is available free of charge on the ACS Publications website at DOI: 10.1021/acs.nanolett.6b00533.

Details for the experimental setup of STM-controlled TERS, the near-field TERS signal extraction, the RBM in TERS spectra, the estimation of TERS enhancement factor, the identification of amorphous carbon impurity cluster, the measurements on the gap-distance dependence of TERS signals, STS data, and the influence of the tip–CNT distance on the TERS spectra (PDF)

■ AUTHOR INFORMATION

Corresponding Author

*E-mail: zcdong@ustc.edu.cn.

Author Contributions

M.L. and S.J. contributed equally.

Notes

The authors declare no competing financial interest.

■ ACKNOWLEDGMENTS

This work is supported by the National Basic Research Program of China, the Strategic Priority Research Program of the Chinese Academy of Sciences, and the National Natural Science Foundation of China.

■ REFERENCES

- (1) Dresselhaus, M. S.; Dresselhaus, G.; Avouris, P., Eds. *Carbon Nanotubes: Synthesis, Structure, Properties and Applications*; Springer: Berlin, Germany, 2001.
- (2) Charlier, J. C. *Acc. Chem. Res.* **2002**, *35*, 1063.
- (3) Wang, M. Z. Carbon Nanotube NEMS. In *Encyclopedia of Nanotechnology*; Bhushan, B., Ed.; Springer: Netherlands, 2015; pp 1–12.
- (4) Anderson, M. S. *Appl. Phys. Lett.* **2000**, *76*, 3130.
- (5) Hayazawa, N.; Inouye, Y.; Sekkat, Z.; Kawata, S. *Opt. Commun.* **2000**, *183*, 333.
- (6) Stöckle, R. M.; Suh, Y. D.; Deckert, V.; Zenobi, R. *Chem. Phys. Lett.* **2000**, *318*, 131.
- (7) Pettinger, B.; Picardi, G.; Schuster, R.; Ertl, G. *Electrochemistry (Tokyo, Jpn.)* **2000**, *68*, 942.
- (8) Pettinger, B.; Schambach, P.; Villagómez, C. J.; Scott, N. *Annu. Rev. Phys. Chem.* **2012**, *63*, 379.
- (9) Schmid, T.; Opilik, L.; Blum, C.; Zenobi, R. *Angew. Chem., Int. Ed.* **2013**, *52*, 5940.
- (10) Zhang, R.; Zhang, Y.; Dong, Z. C.; Jiang, S.; Zhang, C.; Chen, L. G.; Zhang, L.; Liao, Y.; Aizpurua, J.; Luo, Y.; Yang, J. L.; Hou, J. G. *Nature (London, U. K.)* **2013**, *498*, 82.
- (11) Jiang, S.; Zhang, Y.; Zhang, R.; Hu, C. R.; Liao, M. H.; Luo, Y.; Yang, J. L.; Dong, Z. C.; Hou, J. G. *Nat. Nanotechnol.* **2015**, *10*, 865.
- (12) Hartschuh, A.; Sánchez, E. J.; Xie, X. S.; Novotny, L. *Phys. Rev. Lett.* **2003**, *90*, 095503.
- (13) Anderson, N.; Hartschuh, A.; Cronin, S.; Novotny, L. *J. Am. Chem. Soc.* **2005**, *127*, 2533.
- (14) Anderson, N.; Hartschuh, A.; Novotny, L. *Nano Lett.* **2007**, *7*, 577.
- (15) Georgi, C.; Hartschuh, A. *Appl. Phys. Lett.* **2010**, *97*, 143117.
- (16) Yano, T. A.; Ichimura, T.; Kuwahara, S.; H'Dhili, F.; Uetsuki, K.; Okuno, Y.; Verma, P.; Kawata, S. *Nat. Commun.* **2013**, *4*, 2592.
- (17) Yano, T. A.; Verma, P.; Saito, Y.; Ichimura, T.; Kawata, S. *Nat. Photonics* **2009**, *3*, 473.
- (18) Ichimura, T.; Fujii, S.; Verma, P.; Yano, T.; Inouye, Y.; Kawata, S. *Phys. Rev. Lett.* **2009**, *102*, 186101.
- (19) Chen, C.; Hayazawa, N.; Kawata, S. *Nat. Commun.* **2014**, *5*, 3312.
- (20) Yano, T.; Inouye, Y.; Kawata, S. *Nano Lett.* **2006**, *6*, 1269.
- (21) Hartschuh, A.; Qian, H.; Georgi, C.; Böhmeler, M.; Novotny, L. *Anal. Bioanal. Chem.* **2009**, *394*, 1787.
- (22) Johnson, P. B.; Christy, R. W. *Phys. Rev. B* **1972**, *6*, 4370.
- (23) West, P. R.; Ishii, S.; Naik, G. V.; Emani, N. K.; Shalae, V. M.; Boltasseva, A. *Laser Photon. Rev.* **2010**, *4*, 795.
- (24) Albrecht, P. M.; Lyding, J. W. *Appl. Phys. Lett.* **2003**, *83*, 5029.
- (25) Tapasztó, L.; Márk, G. I.; Koós, A. A.; Lambin, P.; Biró, L. P. *J. Phys.: Condens. Matter* **2006**, *18*, 5793.
- (26) Dresselhaus, M. S.; Dresselhaus, G.; Jorio, A.; Souza Filho, A. G.; Saito, R. *Carbon* **2002**, *40*, 2043.
- (27) Dresselhaus, M. S.; Dresselhaus, G.; Saito, R.; Jorio, A. *Phys. Rep.* **2005**, *409*, 47.
- (28) Kim, P.; Odom, T. W.; Huang, J. L.; Lieber, C. M. *Phys. Rev. Lett.* **1999**, *82*, 1225.
- (29) Cançado, L. G.; Beams, R.; Novotny, L. Preprint at <http://arxiv.org/abs/0802.3709>.
- (30) Gupta, A. K.; Russin, T. J.; Gutiérrez, H. R.; Eklund, P. C. *ACS Nano* **2009**, *3*, 45.
- (31) Casiraghi, C.; Hartschuh, A.; Qian, H.; Piscanec, S.; Georgi, C.; Fasoli, A.; Novoselov, K. S.; Basko, D. M.; Ferrari, A. C. *Nano Lett.* **2009**, *9*, 1433.
- (32) Lucchese, M. M.; Stavale, F.; Ferreira, E. H. M.; Vilani, C.; Moutinho, M. V. O.; Capaz, R. B.; Achete, C. A.; Jorio, A. *Carbon* **2010**, *48*, 1592.
- (33) Beams, R.; Cançado, L. G.; Novotny, L. *Nano Lett.* **2011**, *11*, 1177.
- (34) Su, W. T.; Roy, D. J. *Vac. Sci. Technol. B* **2013**, *31*, 041808.
- (35) Beams, R.; Cançado, L. G.; Novotny, L. *J. Phys.: Condens. Matter* **2015**, *27*, 083002.
- (36) Meng, L.; Yang, Z.; Chen, J.; Sun, M. *Sci. Rep.* **2015**, *5*, 9240.
- (37) Zhang, C.; Chen, B. Q.; Li, Z. Y. *J. Phys. Chem. C* **2015**, *119*, 11858.
- (38) Duan, S.; Tian, G. J.; Ji, Y. F.; Shao, J. S.; Dong, Z. C.; Luo, Y. J. *Am. Chem. Soc.* **2015**, *137*, 9515.
- (39) Downes, A.; Salter, D.; Elfick, A. *J. Phys. Chem. B* **2006**, *110*, 6692.
- (40) Zhang, Y. Y.; Zhang, J.; Son, H. B.; Kong, J.; Liu, Z. F. *J. Am. Chem. Soc.* **2005**, *127*, 17156.
- (41) Duan, X.; Son, H. B.; Gao, B.; Zhang, J.; Wu, T. J.; Samsonidze, G. G.; Dresselhaus, M. S.; Liu, Z. F.; Kong, J. *Nano Lett.* **2007**, *7*, 2116.

- (42) Gao, B.; Duan, X. J.; Zhang, J.; Wu, G.; Dong, J. M.; Liu, Z. F. *J. Phys. Chem. C* **2008**, *112*, 10789.
- (43) Cronin, S. B.; Swan, A. K.; Ünlü, M. S.; Goldberg, B. B.; Dresselhaus, M. S.; Tinkham, M. *Phys. Rev. Lett.* **2004**, *93*, 167401.
- (44) Malola, S.; Häkkinen, H.; Koskinen, P. *Phys. Rev. B: Condens. Matter Mater. Phys.* **2008**, *78*, 153409.
- (45) Ren, Y.; Song, L.; Ma, W. J.; Zhao, Y. C.; Sun, L. F.; Gu, C. Z.; Zhou, W. Y.; Xie, S. S. *Phys. Rev. B: Condens. Matter Mater. Phys.* **2009**, *80*, 113412.
- (46) Zhang, C.; Gao, B.; Chen, L. G.; Meng, Q. S.; Yang, H.; Zhang, R.; Tao, X.; Gao, H. Y.; Liao, Y.; Dong, Z. C. *Rev. Sci. Instrum.* **2011**, *82*, 083101.
- (47) Venema, L. C.; Wildöer, J. W. G.; Tuinstra, H. L. J. T.; Dekker, C.; Rinzler, A. G.; Smalley, R. E. *Appl. Phys. Lett.* **1997**, *71*, 2629.
- (48) Jorio, A.; Pimenta, M. A.; Souza Filho, A. G.; Samsonidze, G. G.; Swan, A. K.; Ünlü, M. S.; Goldberg, B. B.; Saito, R.; Dresselhaus, G.; Dresselhaus, M. S. *Phys. Rev. Lett.* **2003**, *90*, 107403.
- (49) Saito, R.; Jorio, A.; Hafner, J. H.; Lieber, C. M.; Hunter, M.; McClure, T.; Dresselhaus, G.; Dresselhaus, M. S. *Phys. Rev. B: Condens. Matter Mater. Phys.* **2001**, *64*, 085312.